Strongly Enhanced Thermoelectric Performance over a Wide Temperature Range in Topological Insulator Thin Films

Te-Hsien Wang

Department of Physics, National Tsing Hua University, Hsinchu 30013, Taiwan

Horng-Tay Jeng*

Department of Physics, National Tsing Hua University, Hsinchu 30013, Taiwan
Physics Division, National Center for Theoretical Sciences, Hsinchu 30013, Taiwan
Institute of Physics, Academia Sinica, Taipei 11529, Taiwan

🅢 *Supporting Information*

ABSTRACT: Thermoelectric (TE) devices have been attracting increasing attention because of their ability to convert heat directly to electricity. To date, improving the TE figure of merit remains the key challenge. The advent of the topological insulator and the emerging nanotechnology open a new way to design high-performance TE devices. By combining first-principles calculations with Boltzmann transport theory, we demonstrate for epitaxial Bi_2Se_3 thin films with thickness slightly larger than six quintuple layers, the relaxation time of the in-gap topological surface states can reach hundreds of femtoseconds, which is 2 orders of magnitude larger than that of the bulk states. Such a strong relaxation time enhancement achieves an approximately 3 times larger electrical- to thermal-conductance ratio than the value predicted by the Wiedemann−Franz law. This condition also enhances the Seebeck coefficient, and consequently leads to the excellent TE figure of merit $zT \sim 2.1$ at room temperature with high TE efficiency over a wide temperature range. The TE performance can be further improved by introducing defects in the bulk-like middle layers of the thin film. The improvement is significant at room temperature and can be even better at a higher temperature. Similar strong enhancement of TE performance is expected in other topological insulator thin films.

KEYWORDS: *thermoelectric, topological insulator, Bi_2Se_3, thin film, Wiedemann−Franz law violation, anomalous Seebeck effect*
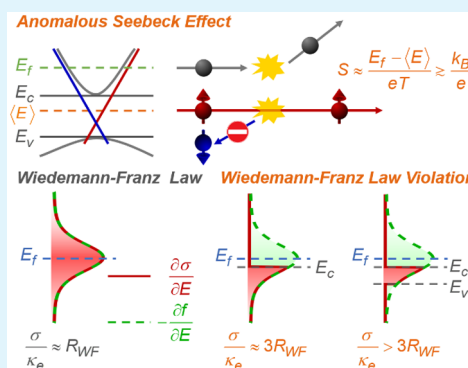
INTRODUCTION

The emerging issue all people face today is the numerous problems relating to energy supply and consumption. Nearly 70% of the world's energy is wasted and dissipated into the environment as low-grade heat.[1] Therefore, thermoelectric (TE) generators, which can convert heat into high-quality electricity, having advantages of solid-state operation without moving parts, no release of greenhouse gases, good stability, and high reliability, have attracted widespread research interest.[2−13] However, the TE devices available to date are still in limited application mainly because of their low energy-conversion efficiency.

The efficiency of the TE devices is determined by the dimensionless figure of merit zT. The TE efficiency approaches the Carnot limit as zT approaches infinity. Theoretically, there is no upper limit on the value of zT. However, to date, no material of $zT > 3$ has been found.[14,15] The main difficulty to improve the figure of merit stems from the trade-off between the TE parameters. The figure of merit can be expressed as

$$zT = \frac{\sigma S^2 T}{\kappa} \tag{1}$$

where T is the absolute temperature, S the Seebeck coefficient, σ the electrical conductivity, and κ the thermal conductivity including the electronic κ_e and lattice κ_L parts. For metals, the electronic thermal conductivity dominates; i.e., $\kappa \sim \kappa_e$. According to the Wiedemann−Franz law, the electrical conductivity is nearly proportional to the thermal conductivity. One cannot increase the electrical conductivity and simultaneously reduce the thermal conductivity. Therefore, the figure of merit is mostly determined by the magnitude of the Seebeck coefficient, which is usually small for metals. For insulators and semiconductors, the lattice thermal conductivity dominates; i.e., $\kappa \sim \kappa_L$. In principle, one can reduce the lattice thermal conductivity without significantly changing the electrical
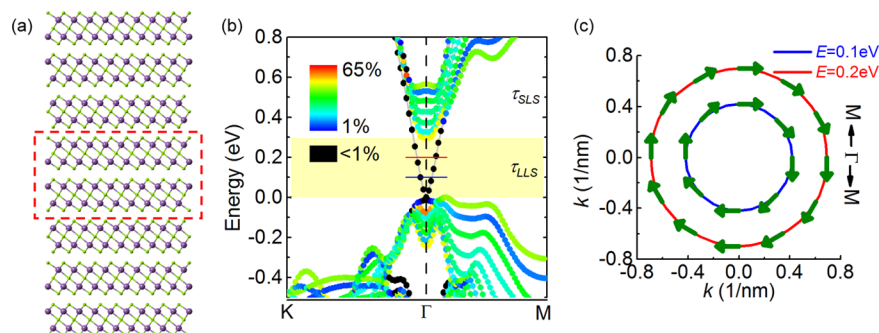
Figure 1. Crystal structure and the electronic band structure of the 8 QL Bi_2Se_3. (a) Cystal structure. The red box indicates the middle 2 QLs, i.e., the bulk region. (b) Electronic band structure. The yellow shaded bulk band gap indicates the energy interval of the LLSs composed of in-gap TSSs. The color of the data points represents the bulk contribution from atoms in the red box in panel a. The black spheres show the TSSs with the bulk contribution (red box in panel a) less than 1%. (c) Spin texture of the constant-energy contours.

conductivity. However, the reduction of the thermal conductivity is usually through introducing all kinds of defects, which would cause a significant reduction in electrical conductivity.[2,16,17] Furthermore, the electrical conductivity increases with carrier concentration while the magnitude of the Seebeck coefficient decreases. Improving the power factor, σS^2, through optimizing the carrier concentration and engineering the band-structure, and therefore achieving high figure of merit over a wide temperature range remain a great challenge.[8]

Topological insulators (TIs), a new class of quantum matter attracting tremendous attention recently, are materials with an inverted bulk band gap induced by the strong spin−orbit coupling with the metallic topological surface states (TSSs) protected by time reversal symmetry.[18−24] Most TIs such as Bi_2Te_3, Sb_2Te_3, and Bi_2Te_2Se are also good TE materials because TI and TE materials usually share two common features, which are not directly related to the TSSs.[25−29] (1) The corrugated constant-energy surfaces with complex band structures caused by band inversions over the mild TI energy gaps can lead to high power factors in TE materials. (2) The large atomic mass with strong spin−orbit coupling for TIs also brings a low lattice thermal conductivity to improve the TE performance. When the size is reduced to the nanometer scale, the TSSs will significantly change the TE performance for both the two-dimensional (2D) and the three-dimensional (3D) TIs.[30,31] Layered bismuth selenide (Bi_2Se_3) is one of the most intensively studied 3D TIs. It has a considerable bulk gap (∼0.3 eV) and topologically protected metallic surface states.[25,32,33] Although the bulk crystalline Bi_2Se_3 is not a good TE material, it has been shown that the TE performance can be greatly enhanced by fabricating a single-layer-based composite made from atomically thick layers.[34]

In this work, through first-principles calculations and the Boltzmann transport theory, we demonstrate, for Bi_2Se_3 thin films with thickness slightly larger than six quintuple layers (QLs), the TE figure of merit zT reaches a remarkably high value of 2.1, which is 2 orders of magnitude larger than the bulk value and is better than that of most good TE materials. The main cause is the extremely high relaxation time of the in-gap TSSs which is about 2 orders of magnitude longer than that of the bulk states. These long relaxation time TSSs can create a high electrical conductivity even though its carrier concentration is low. The high relaxation time ratio at a reasonably low in-gap TSS carrier concentration also leads to a large magnitude of the Seebeck coefficient with an opposite sign to the bulk counterpart. This is the anomalous Seebeck

effect first predicted in a theoretical work[30] and soon been confirmed experimentally.[35] Based on the aforementioned high relaxation time ratio, here we report for the first time another unusual phenomenon: the Wiedemann−Franz law violation. We find the electrical- to electronic thermal-conductivity ratio in Bi_2Se_3 thin films can be ∼3 times larger than the value given by the Wiedemann−Franz law, which was known as a robust law limiting the magnitude of this ratio. The experimental observation of the anomalous Seebeck effect,[35] not only approves our temperature dependence of the Seebeck coefficient for Fermi levels in different energy regions but also supports our calculations that the Wiedemann−Franz law is significantly violated at the same time, as demonstrated in Supporting Information Section SVII. The significant violation of the Wiedemann−Franz law was mostly found in a few strongly correlated systems at cryogenic temperature.[36] Here, the violation of the Wiedemann−Franz law, having nothing to do with the strong correlation, results from the extremely large difference in the relaxation time between the in-gap TSSs and bulk states. This mechanism is not limited to the low temperature and, hence, opens a new way toward the TE power generator operating efficiently over a wide temperature range above the room temperature. Previously this was considered unlikely using a single material.[8,37] The TE performance can be further improved by introducing defects in the bulk-like middle layers. Based on our Bi_2Se_3 thin film study, similar strong enhancement is expected in other 3D TI thin films.

■ RESULTS AND DISCUSSION

Electronic Structure and Electron Scattering. Figure 1b shows the electronic structure of the 8 QL Bi_2Se_3 thin film. The massless Dirac cone lies exclusively within the bulk band gap (yellow shaded region) between the valence band edge (VBE) $E_v = -0.5$ meV and the conduction band edge (CBE) $E_c = 295$ meV. The Dirac cone is composed of doubly degenerate states with the two TSSs on different sides of the film. The wave functions of the TSSs (typically with thickness less than 3 QL as discussed in Supporting Information section SV) on different sides of the film are spatially separated so that the contribution from the bulk-like middle 2 QLs (red box in Figure 1a) is less than 1%. The in-gap TSSs, hereafter denoted by long lifetime states (LLSs), have long relaxation times τ_{LLS} due to two reasons: (i) The large-angle scattering between the TSSs on the same side of the thin film is suppressed because of the chiral spin texture circulating the Γ point as shown in
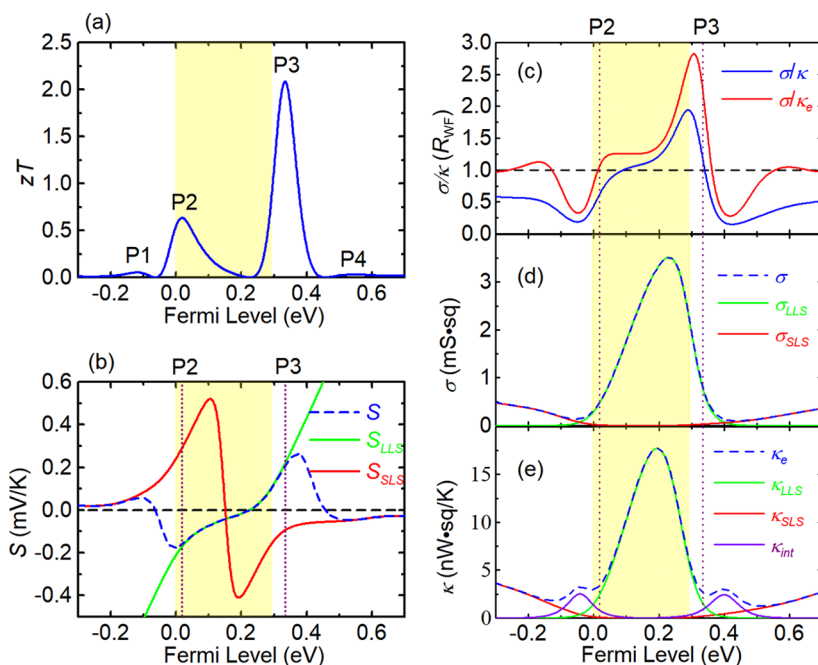
Figure 2. Room-temperature thermoelectric parameters of the 8 QL Bi$_2$Se$_3$ as functions of the Fermi level. (a) Figure of merit zT. The yellow region indicates the bulk band gap. P1−4 denote the four peak energies of zT. (b) Total Seebeck coefficient S and the LLS (SLS) Seebeck coefficient S_{LLS} (S_{SLS}). (c) Ratio of σ to the total (electronic) thermal sheet conductance κ (κ_e). The horizontal dashed line indicates the value given by the Wiedemann−Franz law. (d) Total electrical sheet conductance σ and the LLS (SLS) conductance σ_{LLS} (σ_{SLS}). (e) Electronic thermal conductance κ_e, the LLS (SLS) contribution κ_{LLS} (κ_{SLS}), and the LLS−SLS interaction κ_{int} component. The relaxation times of the LLSs and the SLSs are respectively set as 230 and 1 fs. The vertical dashed lines in panels b−e indicate the P2 and P3 energies.

Figure 1c. (ii) The scattering between the TSSs on the opposite sides of the thin film is negligible because of the spatial separation between the initial and final states. On the other hand, all the other states outside the bulk band gap region, hereafter denoted by short lifetime states (SLSs), have much shorter relaxation times τ_{SLS} because of the significant elastic scattering with the bulk states. The long relaxation time of the LLSs can be evaluated by comparing our computed sheet conductance with the experimental data reported in ref 38 (see Supporting Information Section SI for more details). The estimated τ_{LLS} is 230 fs, which is 2 orders of magnitude higher than that of the bulk relaxation time of ∼2.7 fs.[39] As will be demonstrated later, the coexistence of the LLS and SLS carriers in topological insulator thin films with giant relaxation time differences plays a crucial role toward high-efficiency TE materials. To deal with multiple channel carriers, we adopt the dual relaxation time model, which is a generalization of the conventional constant relaxation time approximation.[30] With this model, the electrical conductance is the sum of the LLS and the SLS conductances,[40] the electronic thermal conductance contains an extra LLS-SLS interaction term, and the Seebeck coefficient is a conductance-weighted average of the Seebeck coefficients as discussed in Method.

Thermoelectric Transport Properties. Based on the previous discussion, it is reasonable to set the relaxation time as 230 and 1 fs for the LLSs and the SLSs, respectively, in the TE parameter calculations. The room-temperature TE figure of merit of the 8 QL Bi$_2$Se$_3$ film as a function of the Fermi level is shown in Figure 2a. There are four zT peaks denoted by P1−P4, among which P1 (P4) is located away from the VBE (CBE) while P2 (P3) is located near the VBE (CBE). Remarkably the TE figure of merit reaches a very high value of $zT \sim 2.1$ at P3, which is 2 orders of magnitude larger than the

bulk value of ∼0.03.[34] This zT value is even larger than those of most good TE materials. The encouragingly high zT clearly demonstrates the capability on improving the TE performance by topological insulator thin films. Moreover, the typical Fermi level of topological insulator Bi$_2$Se$_3$ is close to the CBE, which makes the P3 energy with large zT highly feasible. Around P1 or P4 energy, the conduction carriers are mostly of the SLS type, while around P2 or P3 energy, both the LLS and the SLS carriers are significant to the TE performance. The zT peak values of P2 and P3 are much greater than those of P1 and P4, indicating the importance of the coexistence of both the LLS and SLS carriers. Hereafter we will mainly focus on P2 and P3, and we may only discuss the P3 case because the discussion is similar for the P2 case.

Figure 2b shows the Seebeck coefficient as a function of the Fermi level (E_f). Similar to the typical semiconductor cases, the SLS Seebeck coefficient S_{SLS} is negative for n-type doping ($E_f \gtrsim E_c$) and positive for p-type doping ($E_f \lesssim E_v$). The trend of the Seebeck coefficients can be comprehended by rewriting eq 6 in Method as

$$S_i = \frac{E_f - \langle E \rangle_i}{eT} \qquad (2)$$

where

$$\langle E \rangle_i = \frac{\int_{\Delta_i} d\varepsilon \, E \left(-\frac{\partial f}{\partial \varepsilon}\right) \Sigma}{\int_{\Delta_i} d\varepsilon \left(-\frac{\partial f}{\partial \varepsilon}\right) \Sigma} \qquad (3)$$

is the average energy over the dimensionless differential conductivity (DDC) $(-\partial f/\partial \varepsilon)\Sigma$, $\varepsilon = E/k_B T$ is the reduced energy, and $\Delta_{i=LLS\ (SLS)}$ denotes the LLS (SLS) energy region. Equation 2 shows the Seebeck coefficient is proportional to the
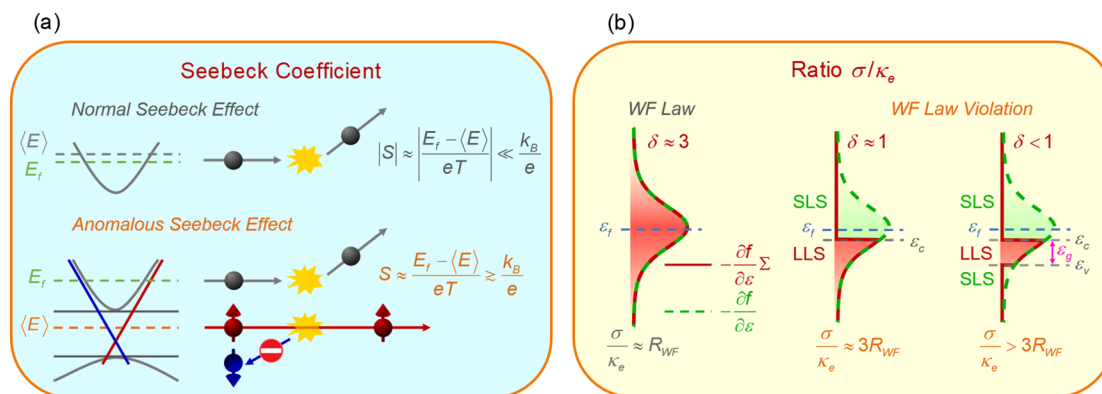
Figure 3. Schematic diagram for the anomalous Seebeck effect and the Wiedemann−Franz law violation. (a) Comparison between normal and anomalous Seebeck effects. (b) DDC profiles $(-\partial f/\partial \varepsilon)\Sigma$ under (left) and beyond (middle and right) the WF law. ε_c (ε_v) is $E_c(E_v)/k_B T$, E_c (E_v) the CBE (VBE), and $\varepsilon_g = \varepsilon_c - \varepsilon_v$ the reduced energy gap.

difference between the DDC averaged energy and the Fermi level. For n-type (p-type) doping, almost all the conduction carriers and hence the $\langle E\rangle_{SLS}$ are slightly higher (lower) than the CBE (VBE) so that the magnitude of S_{SLS} raises as the Fermi level moves toward the midgap. Due to the bipolar effect, the magnitude of the S_{SLS} reduces near the middle of the gap,[40] resulting in the oscillating curve shown in Figure 2b. On the other hand, the LLS Seebeck coefficient S_{LLS} generally has an opposite sign from that of S_{SLS} because the SLS and the LLS conduction carriers distribute at different sides of the Fermi level. The magnitude of the LLS Seebeck coefficient increases as the Fermi level moves away from the LLS energy region. This can be understood by considering eq 2 with the fact that the $\langle E\rangle_{LLS}$ is located in the LLS energy region. As mentioned previously, the Seebeck coefficient is a conductance-weighted average of the LLS and the SLS Seebeck coefficients. With $\tau_{SLS} \ll \tau_{LLS}$ in the present case, the Seebeck coefficient is nearly equal to S_{LLS} in the LLS energy region (yellow shaded), while it approaches S_{SLS} in the SLS energy region (white shaded) above 0.5 eV. At P3 (P2) the resultant Seebeck coefficient is nearly the same as the S_{LLS} with the magnitude of 0.21 (0.16) mV/K. This is slightly larger than the typical value of ∼0.17 mV/K (i.e., $2k_B/e$) for good TE materials without losing the conductivity too much.

Figure 3a shows the schematic diagrams for normal and anomalous Seebeck effects. For most metals, the transport distribution function Σ is nearly a constant within the Fermi window. Thus, the DDC averaged energy $\langle E\rangle$ (eq 3) is very close to E_f, resulting in the normal Seebeck effect with a small negative Seebeck coefficient ($|S| \ll k_B/e$). As for TI thin films, the in-gap TSS, i.e., LLS, carriers well below E_f dominate the electronic transport, while the strong scattering among SLS carriers suppresses the transport around E_f. This acts effectively as an energy filter over carriers enhancing the difference between $\langle E\rangle$ and E_f, and hence leads to the anomalous Seebeck effect with a large positive Seebeck coefficient ($S \gtrsim k_B/e$).

The ratio of the electrical conductance to the electronic thermal conductance σ/κ_e as a function of the Fermi level is shown in Figure 2c. It is normalized in unit of $R_{WF} = 3e^2/\pi^2 k_B^2 T$ given by the Wiedemann−Franz law[41] as indicated by the horizontal dashed line. In general the Wiedemann−Franz law is approximately applicable (i.e., $\sigma/\kappa_e \sim R_{WF}$). Nevertheless the ratio strongly fluctuates near the band edges with a maximum value of about $3 R_{WF}$ around P3 much larger than unity as predicted by the Wiedemann−Franz law. This is

excellent for high TE efficiency that one can take advantage of. As analyzed in Method, the ratio σ/κ_e can be approximated by

$$\frac{\sigma}{\kappa_e} \approx R_{WF}\left[1 + \frac{\pi^2}{3}\left(\frac{k_B T \sigma'}{\sigma}\right)^2 - \frac{8\pi^2}{15}\frac{(k_B T)^2 \sigma''}{\sigma}\right] \quad (4)$$

where the first term is just the Wiedemann−Franz law. In the present case the higher order terms are significant because the relaxation time of the electrons near the band edge and the corresponding dimensionless transport distribution function[42] (see Method) vary rapidly with energy. In the energy region slightly below the CBE, the electrical conductance decreases rapidly with energy. The second term becomes significant, and the ratio σ/κ_e increases to a value much larger than R_{WF}. For the energy region higher than P3, the dominant conduction carriers changes from the LLS to the SLS types, and the sign of the σ' changes from negative to positive. The decreasing magnitude of σ' with a considerable positive σ'' thus leads σ/κ_e to a much smaller value than R_{WF}.

The Wiedemann−Franz law violation can be understood by simplifying the ratio σ/κ_e from eqs 6 and 8 in Method as

$$\frac{\sigma}{\kappa_e} = \frac{\pi^2}{3}\frac{R_{WF}}{\delta} \quad (5)$$

where the variance $\delta = \langle \varepsilon^2\rangle - \langle\varepsilon\rangle^2$ indicates the DDC broadening along the reduced energy ε (eq 3). Note that here δ is the only factor determining the violation of the Wiedemann−Franz law. For most cases as depicted in the left part of Figure 3b, the transport distribution function (Σ) is insensitive to energy around E_f, and the DDC profile $((-\partial f/\partial\varepsilon)\Sigma)$ is nearly the same as that of the Fermi window function $(-\partial f/\partial\varepsilon)$. The variance $\delta \approx \pi^2/3$ simply leads to the Wiedemann−Franz law: $\sigma/\kappa_e \approx R_{WF}$. As for TI thin films shown in the middle part of Figure 3b, the large relaxation time difference between LLSs and SLSs strongly reduces the DDC profile to nearly zero when $\varepsilon > \varepsilon_c$. The typical condition $E_f - E_c \gtrsim k_B T$ in TIs leads the DDC close to an exponential decay function below ε_c. Thus, the nearly unity DDC variance δ results in the ratio σ/κ_e approximately 3 times larger than R_{WF}. On the other hand, shown in the right part of Figure 3b, the SLSs below VBE truncate the DDC tail and result in the narrow DDC profile within the reduced gap ε_g, leading to a higher σ/κ_e ratio. As discussed later, the ratio σ/κ_e is further enhanced at high temperatures because of the suppressed ε_g given by the inverse dependence of temperature ($\varepsilon_g = E_g/k_B T$).
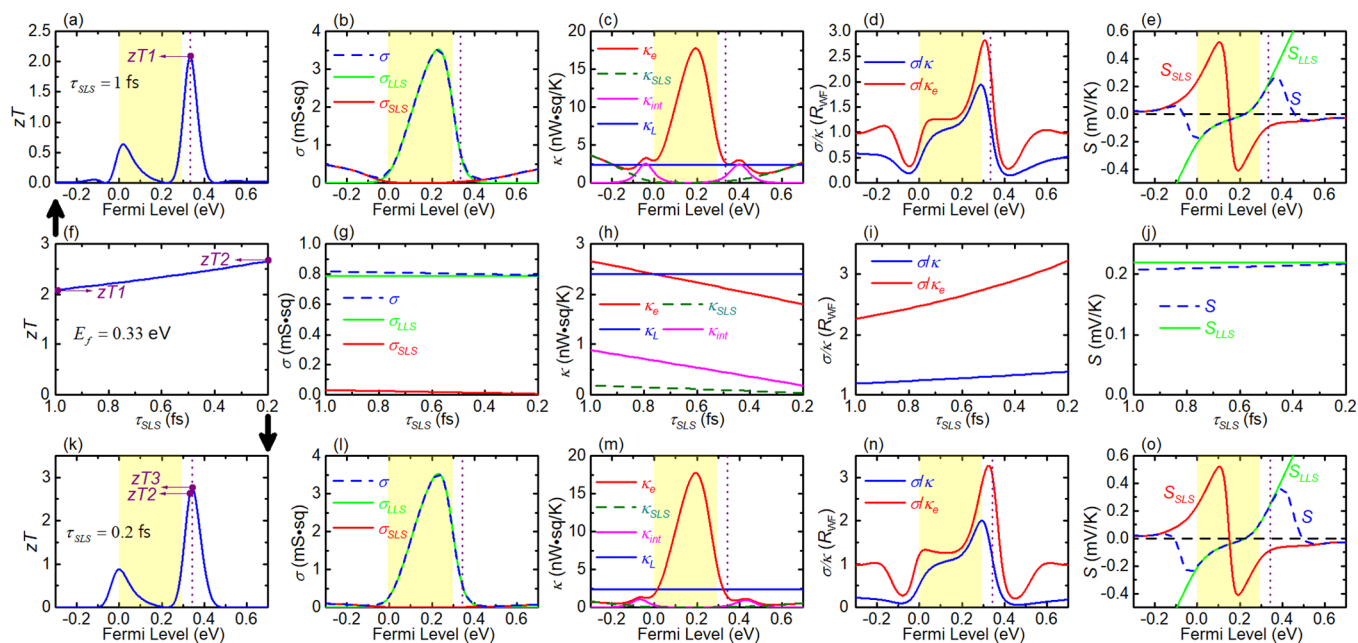
Figure 4. Thermoelectric parameters of the 8 QL Bi_2Se_3 at room temperature $T = 300$ K. (a–e) Thermoelectric parameters as functions of the Fermi level with the SLS relaxation time $\tau_{SLS} = 1$ fs and (k–o) $\tau_{SLS} = 0.2$ fs. The vertical dashed lines in panels a–e and k–o indicate the corresponding P3 energies. The reduced $\tau_{SLS} = 0.2$ fs causes a noticeable blue shift of P3 energy in panel k. In panels a and k, $zT1 = 2.1$ and $zT3 = 2.8$ are, respectively, the zT peak values at P3 for $\tau_{SLS} = 1$ fs and $\tau_{SLS} = 0.2$ fs cases. (f–j) Evolutions of thermoelectric parameters as functions of SLS relaxation time with the Fermi level at 0.33 eV. The P3 energy for $\tau_{SLS} = 1$ fs. The value of $zT2$ in panels f and k is 2.7.
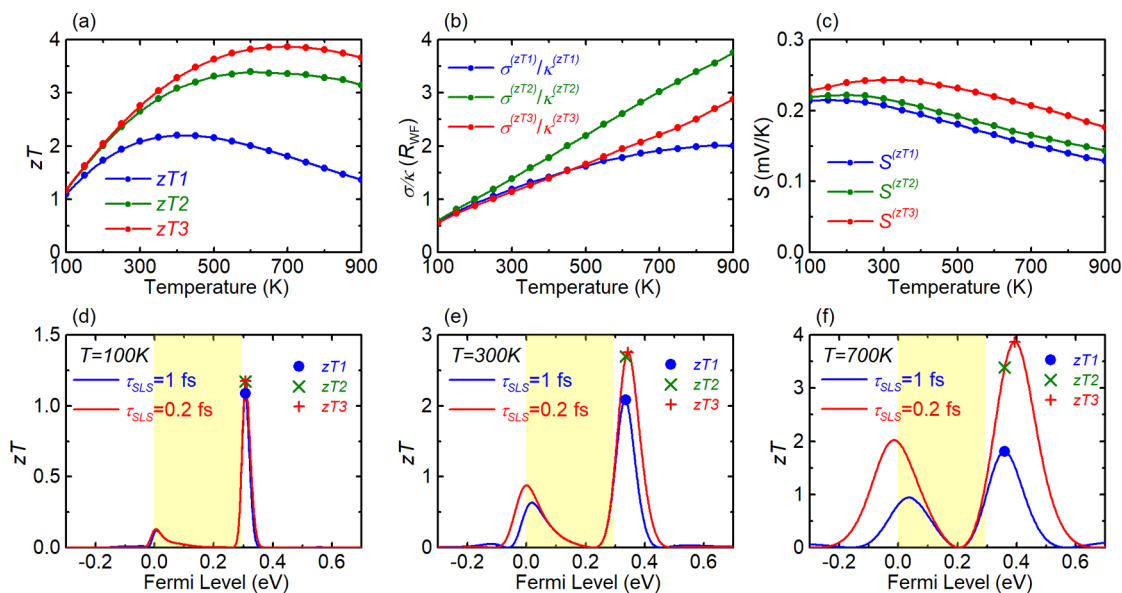
Figure 5. Temperature-dependence of TE parameters of the 8 QL Bi_2Se_3. (a) Figure of merit zT as a function of temperature. $zT1$ ($zT3$) is the P3 figure of merit for $\tau_{SLS} = 1$ fs ($\tau_{SLS} = 0.2$ fs). $zT2$ is for $\tau_{SLS} = 0.2$ fs while the Fermi level is set at the P3 energy of $zT1$. (b) Ratios of electrical-to-thermal conductance and (c) Seebeck coefficient as a function of temperature. (d–f) Figure of merit as a function of Fermi level for (d) $T = 100$ K, (e) $T = 300$ K, and (f) $T = 700$ K.

Figure 2d shows the electrical sheet conductance as a function of the Fermi level. As mentioned previously, the relaxation time of the in-gap TSSs is about 2 orders of magnitude longer than that of the bulk states. A high LLS electrical conductance σ_{LLS} can thus be created. Within the bulk band gap, the total conductance is nearly equal to the LLS conductance due to the lack of SLS carriers. The conductance increases with the Fermi level up to the maximum value at 65 meV below the CBE because of the increasing LLS density of states (DOS). It then decreases because of the reduced

number of LLS conduction carriers regardless of the increase in that of the SLSs. When the Fermi level locates at the P3 energy (42 meV above CBE), the conduction carrier number of the SLSs is much larger than that of the LLSs. Nevertheless, the total conductance is still mainly contributed from the LLS conductance σ_{LLS} because of the large relaxation time of the LLSs. Above 0.5 eV the SLS carriers dominate the transport property; thus, the total conductance is nearly equal to the SLS conductance.
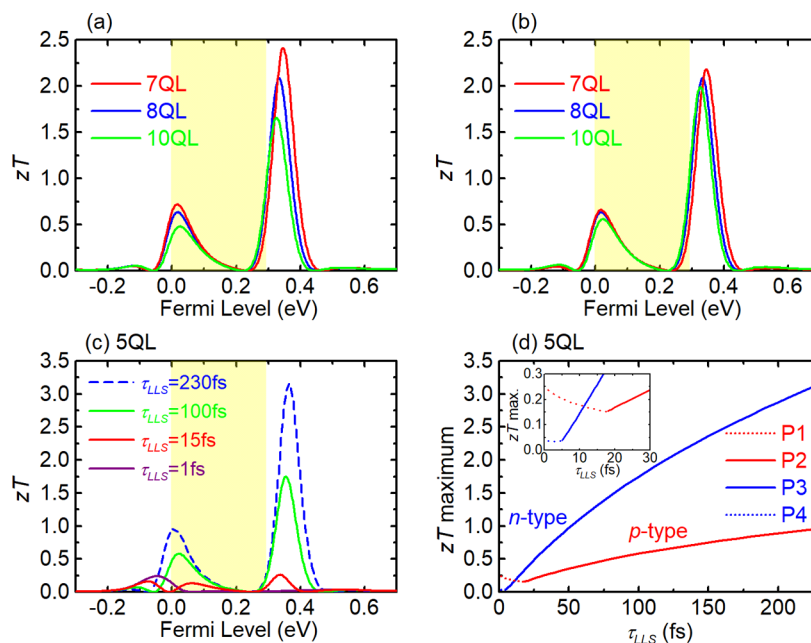
Figure 6. Thickness dependence of the figure of merit in the Bi_2Se_3 thin films at room temperature. (a) Figure of merit as a function of Fermi level for the films of different thickness. (b) Same as panel a except that the lattice thermal conductance of all the films is set at the value of the 8 QL film. The relaxation time of the LLSs (SLSs) in panels a and b is 230 fs (1 fs). (c) Figure of merit of the 5 QL film at temperature $T = 300$ K with different τ_{LLS} as a function of the Fermi level. Blue dashed curve with $\tau_{LLS} = 230$ fs is highly unlikely while the green curve with $\tau_{LLS} = 100$ fs is more realistic for 5 QL film. (d) zT maximum of the 5 QL film at temperature $T = 300$ K as a function of the LLS relaxation time for n-type (p-type) doping.

As analyzed in Method, the interaction between LLS and SLS carriers causes an additional thermal conductance term κ_{int}. This term is significant when the SLS conductance is comparable to the LLS conductance. Interesting effects can be seen in Figure 2e, in which κ_{int} shows two bumps larger than both the κ_{LLS} and the κ_{SLS} around $E_f = -0.05$ and 0.4 eV due to the LLS−SLS interaction. This is also the reason why the ratio σ/κ_e exhibits two minimum values at the corresponding energies.

Further Enhancement by Shortening the SLS Relaxation Time. The TE performance can be further enhanced by introducing defects in the bulk-like middle layers to reduce the SLS relaxation time without changing the LLS relaxation time. Figure 4 demonstrates the strengthened TE parameters at temperature $T = 300$ K by shortening τ_{SLS} from 1 fs (Figure 4a−e) to 0.2 fs (Figure 4k−o) and their evolutions (Figure 4f−j). The remarkable increase in the figure of merit at P3 energy from $zT1 = 2.1$ (Figure 4a) to $zT2 = 2.7$ (Figure 4f,k) are clearly shown. This is accomplished by the notable growing σ/κ_e ratio (Figure 4i) associated with the slightly increasing Seebeck coefficient (Figure 4j) at P3. In the short $\tau_{SLS} = 0.2$ fs limit, even stronger violation of the Wiedemann−Franz law can be seen in Figure 4d,i,n. The maximum ratio over 3 times larger than the value expected from the Wiedemann−Franz law plays the crucial role on boosting the figure of merit presented in Figure 4f. The origin of this extraordinarily high σ/κ_e ratio at P3 energy is the prominent reduction in κ_{int} and therefore κ_e (Figure 4c,h,m) due to the shortened $\tau_{SLS} = 0.2$ fs. On the other hand, there is no corresponding LLS−SLS interaction counterpart electrical conductance. The SLS conductance remains negligible as shown in Figure 4b,g,l. This diminished σ_{SLS} is the source of the slightly raised Seebeck coefficient (Figure 4j) according to eq 16 (Method) under the circumstances that the S_{LLS} and S_{SLS}

remain the same with $\tau_{SLS} = 2$ or 0.2 fs (Figure 4e,o). Finally the reduction of the SLS relaxation time also results in the blue shift of the P3 energy causing a further enhancement of the figure of merit to $zT3 = 2.8$ (Figure 4k).

Temperature Dependence of the TE Performance. The temperature dependence of the TE parameters is an important factor in realistic applications. In general, the figure of merit increases with temperature, reaches its maximum, and then decreases at high temperature. As illustrated in Figure 5a, our $zT1$ curve for undefected Bi_2Se_3 8 QL thin film increases from 1.1 at 100 K to 2.1 at 300 K with the maximum value of 2.2 around 400 K. This figure of merit curve is indeed excellent as compared with other good TE materials. Not only the room-temperature TE efficiency is remarkably high but also can be made better at higher temperatures. One can achieve a better $zT2$ curve and an even higher blue-shifted $zT3$ performance by proper defects with the maxima zT 3.4 and 3.9 located at 600 and 700 K, respectively. Detailed zT spectra at 100, 300, and 700 K are depicted in Figure 5d−f, among which Figure 5f shows the best zT curve obtained in this work. In addition, the larger zT spectral width at higher temperatures yields a wider energy window for experimentally tuning the Fermi level. Even at room temperature, an excellent zT value ranging from 2.1 ($zT1$) to 2.8 ($zT3$) can be reached if τ_{SLS} is reduced from 1 fs (undefected) to 0.2 fs (defected). The enhancement by the defects in the bulk-like middle layers ($zT2$, $zT3$) is weak at low temperature, significant at room temperature, and more pronounced at high temperature. As mentioned previously, to achieve high TE efficiency over a wide temperature range using a single material remains a great challenge.[3,8] Such outstanding TE performance of Bi_2Se_3 thin films over a wide temperature range provides an ideal solution to this issue. Supporting Information Section SVI demonstrates that the corresponding TE device efficiency based on Bi_2Se_3

thin films can be higher than 35% of the Carnot efficiency operating over a wide temperature range with $\Delta T \sim 600$ K,[43] which is much larger than 24% of typical good ($zT \sim 1$) TE materials, for example Bi_2Te_3, over $\Delta T \sim 300$ K.[3,8]

The ratio σ/κ in unit of R_{WF} overall increases with temperature as shown in Figure 5b. This is the reason why at low temperatures zT increases with increasing temperature. At low temperatures, the thermal conductance mainly comes from its lattice component causing the ratio σ/κ much smaller than one R_{WF}. Because κ_L (κ_e) decreases (increases) with temperature, σ/κ increases and approaches its upper bound σ/κ_e as discussed in Supporting Information Section SII. The σ/κ ratio is therefore increasing along with temperature as shown in Figure 5b. In addition, the ratio $\sigma^{(zT2)}/\kappa^{(zT2)}$ can be significantly larger than $3R_{WF}$ when $T > 700$ K. The $\sigma^{(zT2)}/\kappa_e^{(zT2)}$ and the maximum σ/κ_e, as shown in Figures S2 and S3, can be $\sim$5 times larger than the R_{WF}, indicating that a considerable portion of DDC profile is cut by the SLSs below VBE as discussed previously. On the other hand, the magnitude of the Seebeck coefficient (Figure 5c) decreases with temperature above 300 K because of the T term in the denominator of eq 2. As a result, the zT curves (Figure 5a) raise at low temperature and decline at high temperature with the maximum values significantly above the room temperature (see Supporting Information section SII for detailed discussion).

Thickness Dependence of the TE Performance. Figure 6a shows the figure of merit of the 7, 8, and 10 QL Bi_2Se_3 thin films at room temperature. The figure of merit at P2 and P3 decreases with the increasing film thickness significantly. To resolve the origin of the thickness dependence of zT, we depict in Figure 6b these zT curves using the same lattice thermal conductance κ_L of the 8 QL film for all three cases. The similar zT peak heights in Figure 6b indicate that the better TE performance in thinner films (Figure 6a) is mainly due to the decreasing lattice thermal conductance κ_L in thinner films. However, for thicker films, it is easier to achieve the lower SLS relaxation time and the higher TE performance by introducing defects into the middle layers as mentioned earlier. Therefore, the optimized film thickness would be the thinnest film that one can introduce defects into the middle bulk-like layers, while the film is still thicker than 6 QLs as discussed below.

For thinner Bi_2Se_3 films less than 6 QLs, the LLS relaxation time is dramatically reduced by the scattering between the TSSs on the opposite sides because the typical decay length of the TSSs is about 3 QLs. Introducing defects into the thin film will significantly reduce not only the SLS relaxation time τ_{SLS} but also the LLS relaxation time τ_{LLS}. Figure 6c shows the figure of merit of the 5 QL Bi_2Se_3 thin film for different τ_{LLS} at temperature $T = 300$ K. The long LLS relaxation time of $\tau_{LLS} = 230$ fs given from the ideal nonoverlap TSSs for thicker films is highly unlikely for the 5 QL case and is thus depicted in a blue dashed curve. The significantly suppressed green zT curve with a smaller maximum value of 1.7 given from τ_{LLS} of 100 fs is much more realistic for 5 QL Bi_2Se_3. Figure 6d shows the corresponding zT maximum at P3, P4 (n-type) and P2, P1 (p-type) as a function of the LLS relaxation time. In general the figure of merit decreases with decreasing LLS relaxation time. For n-type doping, the zT maximum reduces from 3.2 to 0.04 when the LLS relaxation time decreases from 230 to 5 fs. Similar behavior can also be seen for the p-type doping. If we further decrease the LLS relaxation time, then the figure of

merit at P3 (P2) would be smaller than that at P4 (P1) as shown in Figure 6d.

CONCLUSIONS

In summary, we investigate the TE properties of the Bi_2Se_3 thin film through first-principles calculations and the Boltzmann transport theory. With suitable film thickness slightly larger than 6 QLs that the coupling between the TSSs on the opposite sides of the film is negligible, the large-angle scattering is strongly suppressed and the relaxation time of the in-gap TSSs can be hundreds of times longer than that of the bulk states. The strong difference in the relaxation time leads to a high electrical- to electronic thermal-conductance ratio about 3 times larger than the value given by the Wiedemann–Franz law, and a large Seebeck coefficient as well. These combined effects thus give rise to a greatly improved figure of merit over a wide temperature range in Bi_2Se_3 thin film with $zT \sim 2.1$ at room temperature. The TE performance can be further enhanced by reducing the bulk state relaxation time without changing the in-gap TSS one through introducing defects in the bulk-like middle layers. This enhancement is prominent especially at high temperature. For thicker (≥ 10 QLs) films, the figure of merit decreases due to the increasing thermal conductance, while for thinner (≤ 6 QLs) films the significant coupling between TSSs greatly deteriorates the TE performance. The optimal film thickness is approximately 7–10 QLs with suitable defects in the bulk-like middle layers. Although we only consider the Bi_2Se_3 thin film, the excellent TE performance caused by the coexistence of long and short lifetime conduction carriers should be seen in other TI thin films and nanostructures of different morphologies. Experimentally, $\sim$13 times zT enhancement has been observed in the $Bi_{1.5}Sb_{0.5}Te_{1.7}Se_{1.3}$ nanowire in comparison with its bulk specimen.[44] We believe the unconventional TE behaviors and high TE performances demonstrated in this work can be observed in nanostructures of variant morphologies such as that reported in ref 44.

METHOD

Electronic Structure. The electronic structure is calculated through the projector augmented wave (PAW) approach within the framework of density functional theory (DFT) as implemented in the Vienna Ab initio Simulation Package (VASP).[45−47] The exchange–correlation is described in the Perdew–Burke–Ernzerhof (PBE) form of generalized gradient approximation (GGA).[48,49] The spin–orbit coupling is taken into account. The $13 \times 13 \times 1$ Monkhorst–Pack mesh is used for k-point sampling within the Brillouin zone. The cutoff energy for plane wave basis is set as 450 eV. The energy convergence threshold is set to 10^{-9} eV in the self-consistent calculation. For structure relaxation, the van der Waals interactions between two adjacent quintuple layers are included using the DFT-D3 method with Becke–Jonson damping.[50,51] All the internal atomic coordinates and the lattice constant are relaxed until the magnitude of the force acting on all atoms is less than 0.5 meV/Å.

Transport Properties. For the thin film in which the applied field is along the in-plane direction, the figure of merit can be expressed by eq 1, where σ is the electrical sheet conductance and κ the thermal sheet conductance containing the electronic κ_e and lattice κ_L parts. Except for the lattice thermal conductance κ_L that we calculate through the Callaway's model as will be discussed later, all the TE parameters can be obtained from the Boltzmann transport equation with the relaxation time approximation based on our codes. They can be expressed as

$$\sigma = \frac{e^2}{\hbar} I_0 \qquad (6)$$

$$S = -\frac{k_B}{e} \frac{I_1}{I_0} \qquad (7)$$

$$\kappa_e = \frac{k_B^2 T}{\hbar}\left(I_2 - \frac{I_1^2}{I_0}\right) \qquad (8)$$

where e is the elementary charge, k_B the Boltzmann constant, and $\hbar$ the reduced Planck constant. I_n is a dimensionless integral which can be written as

$$I_n = \int d\varepsilon \left(-\frac{\partial f_0}{\partial \varepsilon}\right)(\varepsilon - \varepsilon_f)^n \Sigma \qquad (9)$$

where $f_0 = 1/[\exp(\varepsilon - \varepsilon_f) + 1]$ is the Fermi−Dirac distribution function, $\varepsilon_f = E_f/k_B T$ the reduced Fermi level, and E_f the Fermi level. Σ is the dimensionless transport distribution function,[42] which can be expressed as

$$\Sigma = \frac{\hbar}{(2\pi)^2} \int d^2k \, \delta(E - E_\mathbf{k}) v_\mathbf{k}^2 \tau_\mathbf{k} \qquad (10)$$

where $E_\mathbf{k}$ is the electronic band structure obtained from the DFT calculations, $v_\mathbf{k}$ the group velocity in the direction of the applied field, and $\tau_\mathbf{k}$ the relaxation time.

The lattice thermal conductance κ_L can be obtained through Callaway's model. It can be expressed as[52,53]

$$\kappa_L = \frac{k_B d}{2\pi^2 v_s}\left(\frac{k_B T}{\hbar}\right)^3 \int_0^{T_D/\sqrt[3]{5} T} dy \, \tau_c \frac{y^4 e^y}{(e^y - 1)^2} \qquad (11)$$

where d is the film thickness, v_s the sound velocity, T_D the Debye temperature, $y = \hbar\omega/k_B T$ the dimensionless parameter proportional to the phonon frequency ω. The τ_c is the phonon scattering relaxation time, which can be written as

$$\tau_c^{-1} = \frac{v_s}{d} + A\omega^4 + B\omega^2 T \exp\left(-\frac{T_D}{CT}\right) \qquad (12)$$

where $A = 9.42 \times 10^{-42}$ (s^3), $B = 7.78 \times 10^{-18}$ (sK^{-1}), and $C = 2.8$ are parameters independent of temperature given from ref 53. The three terms of eq 12 represent, respectively, the boundary scattering, the point defect (Rayleigh) scattering, and the phonon−phonon scattering. In ref 53, the Bi$_2$Se$_3$ specimens are single crystals without intentionally introduced defects. Therefore, our lattice thermal conductance calculated from parameters of ref 53 should be considered as the upper bound of that in our defected model. The overestimated lattice thermal conductance would lead to an underestimation of our TE performance. By introducing defects into the bulk-like middle layers, the defect-induced lattice thermal conductance suppression would further enhance our presented TE performance.

Transport Properties Based on the Dual Relaxation Time Model. To calculate the transport properties for multiple channels LLSs and SLSs, we adopt the dual relaxation time model, which is a generalization of the conventional constant relaxation time approximation.[30] In this model, the relaxation times τ_{LLS} and τ_{SLS} are two constants. The integral I_n is divided into the LLS part I_n^{LLS} and the SLS part I_n^{SLS}. Then we can define the LLS (SLS) electrical conductance σ_{LLS} (σ_{SLS}), the LLS (SLS) Seebeck coefficient S_{LLS} (S_{SLS}), and the LLS (SLS) electronic thermal conductance κ_{LLS} (κ_{SLS}) by the equations the same as eqs 6−8, where the integral is replaced by the I_n^{LLS} (I_n^{SLS}). According to this definition, the electrical conductance is the sum of the LLS and the SLS conductances,[40]

$$\sigma = \sigma_{LLS} + \sigma_{SLS} \qquad (13)$$

The electronic thermal conductance, unlike the case of the electrical conductance, is not merely the sum of the LLS and the SLS contributions. It can be expressed as

$$\kappa_e = \kappa_{LLS} + \kappa_{SLS} + \kappa_{int} \qquad (14)$$

where κ_{int} is nonnegative and can be written as

$$\kappa_{int} = \frac{(I_1^{LLS}I_0^{SLS} - I_1^{SLS}I_0^{LLS})^2}{(I_0^{SLS} + I_0^{LLS})I_0^{LLS}I_0^{SLS}} \qquad (15)$$

The cause of κ_{int} is similar to that in the bipolar effect,[40] in which additional thermal conductance appears due to the interaction between electrons and holes. In the present case, the κ_{int} is caused by the interaction between the LLS carriers and the SLS carriers.

On the other hand, the Seebeck coefficient is a conductance-weighted average of the Seebeck coefficients associated with the two type of carriers,

$$S = \frac{\sigma_{LLS}S_{LLS} + \sigma_{SLS}S_{SLS}}{\sigma_{LLS} + \sigma_{SLS}} \qquad (16)$$

Wiedemann−Franz Law and the Higher Order Terms. The Wiedemann−Franz law can be derived by applying the Sommerfeld expansion on eq 9 and retaining the lowest nonvanishing order.[41] By taking into account the higher order terms and replacing Σ with $\int d\varepsilon \left(-\frac{\partial f_0}{\partial \varepsilon}\right)\Sigma$, the ratio of the electrical conductance to the electronic thermal conductance σ/κ_e can be approximated by

$$\frac{\sigma}{\kappa_e} \approx R_{WF}\left[1 + \frac{\pi^2}{3}\left(\frac{k_B T \sigma'}{\sigma}\right)^2 - \frac{8\pi^2}{15}\frac{(k_B T)^2 \sigma''}{\sigma}\right] \qquad (17)$$

where the prime denotes the derivative with respect to E_f. Here the first term is just the Wiedemann−Franz law.

■ ASSOCIATED CONTENT

ⓈSupporting Information

The Supporting Information is available free of charge on the ACS Publications website at DOI: 10.1021/acsaem.8b01188.

Estimation of the LLS relaxation time, details of TE parameters temperature dependences, further violation of Wiedemann−Franz law, TE performance in the limit of large LLS relaxation time, charge density distribution, TE efficiency of TE generators, and temperature dependences of Seebeck coefficient and of electronic scattering (PDF)

■ AUTHOR INFORMATION

Corresponding Author

*E-mail: jeng@phys.nthu.edu.tw.

ORCID ⦿

Horng-Tay Jeng: 0000-0002-2881-3826

Notes

The authors declare no competing financial interest.

■ REFERENCES

(1) Zevenhoven, R.; Beyene, A. The Relative Contribution of Waste Heat from Power Plants to Global Warming. *Energy* **2011**, *36*, 3754−3762.

(2) Rowe, D. M. *CRC Handbook of Thermoelectrics*; CRC Press: Boca Raton, FL, USA, 1995.

(3) Tritt, T. M.; Subramanian, M. A. Thermoelectric Materials, Phenomena, and Applications: A Bird's Eye View. *MRS Bull.* **2006**, *31*, 188−194.

(4) Snyder, G. J. Small Thermoelectric Generators. *Electrochem. Soc. Interface* **2008**, *17*, 54−56.

(5) Tritt, T. M. Thermoelectric Phenomena, Materials, and Applications. *Annu. Rev. Mater. Res.* **2011**, *41*, 433−448.

(6) Alam, H.; Ramakrishna, S. A Review on the Enhancement of Figure of Merit from Bulk to Nano-Thermoelectric Materials. *Nano Energy* **2013**, *2*, 190−212.

(7) He, W.; Zhang, G.; Zhang, X. X.; Ji, J.; Li, G. Q.; Zhao, X. D. Recent Development and Application of Thermoelectric Generator and Cooler. *Appl. Energy* **2015**, *143*, 1−25.

(8) Aswal, D. K.; Basu, R.; Singh, A. Key Issues in Development of Thermoelectric Power Generators: High Figure-of-Merit Materials and Their Highly Conducting Interfaces with Metallic Interconnects. *Energy Convers. Manage.* **2016**, *114*, 50−67.

(9) Zhang, Q. H.; Huang, X. Y.; Bai, S. Q.; Shi, X.; Uher, C.; Chen, L. D. Thermoelectric Devices for Power Generation: Recent Progress and Future Challenges. *Adv. Eng. Mater.* **2016**, *18*, 194−213.

(10) Su, X. L.; Wei, P.; Li, H.; Liu, W.; Yan, Y. G.; Li, P.; Su, C. Q.; Xie, C. J.; Zhao, W. Y.; Zhai, P. C.; Zhang, Q. J.; Tang, X. F.; Uher, C. Multi-Scale Microstructural Thermoelectric Materials: Transport Behavior, Non-Equilibrium Preparation, and Applications. *Adv. Mater.* **2017**, *29*, 1602013.

(11) Siddique, A. R. M.; Mahmud, S.; Van Heyst, B. A Review of the State of the Science on Wearable Thermoelectric Power Generators (TEGs) and Their Existing Challenges. *Renewable Sustainable Energy Rev.* **2017**, *73*, 730−744.

(12) Ali, A.; Chen, Y. X.; Vasiraju, V.; Vaddiraju, S. Nanowire-Based Thermoelectrics. *Nanotechnology* **2017**, *28*, 282001.

(13) Zhao, W.; Liu, Z.; Sun, Z.; Zhang, Q.; Wei, P.; Mu, X.; Zhou, H.; Li, C.; Ma, S.; He, D.; Ji, P.; Zhu, W.; Nie, X.; Su, X.; Tang, X.; Shen, B.; Dong, X.; Yang, J.; Liu, Y.; Shi, J. Superparamagnetic Enhancement of Thermoelectric Performance. *Nature* **2017**, *549*, 247−251.

(14) Zhao, L. D.; Lo, S. H.; Zhang, Y. S.; Sun, H.; Tan, G. J.; Uher, C.; Wolverton, C.; Dravid, V. P.; Kanatzidis, M. G. Ultralow Thermal Conductivity and High Thermoelectric Figure of Merit in SnSe Crystals. *Nature* **2014**, *508*, 373−377.

(15) Dewandre, A.; Hellman, O.; Bhattacharya, S.; Romero, A. H.; Madsen, G. K. H.; Verstraete, M. J. Two-Step Phase Transition in SnSe and the Origins of Its High Power Factor from First Principles. *Phys. Rev. Lett.* **2016**, *117*, 276601.

(16) Biswas, K.; He, J. Q.; Blum, I. D.; Wu, C. I.; Hogan, T. P.; Seidman, D. N.; Dravid, V. P.; Kanatzidis, M. G. High-Performance Bulk Thermoelectrics with All-Scale Hierarchical Architectures. *Nature* **2012**, *489*, 414−418.

(17) Zhao, L. D.; Dravid, V. P.; Kanatzidis, M. G. The Panoscopic Approach to High Performance Thermoelectrics. *Energy Environ. Sci.* **2014**, *7*, 251−268.

(18) Kane, C. L.; Mele, E. J. Z(2) Topological Order and the Quantum Spin Hall Effect. *Phys. Rev. Lett.* **2005**, *95*, 146802.

(19) Bernevig, B. A.; Zhang, S. C. Quantum Spin Hall Effect. *Phys. Rev. Lett.* **2006**, *96*, 106802.

(20) Fu, L.; Kane, C. L.; Mele, E. J. Topological Insulators in Three Dimensions. *Phys. Rev. Lett.* **2007**, *98*, 106803.

(21) Moore, J. E.; Balents, L. Topological Invariants of Time-Reversal-Invariant Band Structures. *Phys. Rev. B: Condens. Matter Mater. Phys.* **2007**, *75*, 121306.

(22) Qi, X.-L.; Hughes, T. L.; Zhang, S. C. Topological Field Theory of Time-Reversal Invariant Insulators. *Phys. Rev. B: Condens. Matter Mater. Phys.* **2008**, *78*, 195424.

(23) Hasan, M. Z.; Kane, C. L. Colloquium: Topological Insulators. *Rev. Mod. Phys.* **2010**, *82*, 3045−3067.

(24) Bansil, A.; Lin, H.; Das, T. Colloquium: Topological Band Theory. *Rev. Mod. Phys.* **2016**, *88*, 021004.

(25) Zhang, H. J.; Liu, C. X.; Qi, X. L.; Dai, X.; Fang, Z.; Zhang, S. C. Topological Insulators in Bi_2Se_3, Bi_2Te_3 and Sb_2Te_3 with a Single Dirac Cone on the Surface. *Nat. Phys.* **2009**, *5*, 438−442.

(26) Chen, Y. L.; Analytis, J. G.; Chu, J. H.; Liu, Z. K.; Mo, S. K.; Qi, X. L.; Zhang, H. J.; Lu, D. H.; Dai, X.; Fang, Z.; Zhang, S. C.; Fisher, I. R.; Hussain, Z.; Shen, Z. X. Experimental Realization of a Three-Dimensional Topological Insulator, Bi_2Te_3. *Science* **2009**, *325*, 178−181.

(27) Xie, W. J.; He, J.; Kang, H. J.; Tang, X. F.; Zhu, S.; Laver, M.; Wang, S. Y.; Copley, J. R. D.; Brown, C. M.; Zhang, Q. J.; Tritt, T. M. Identifying the Specific Nanostructures Responsible for the High Thermoelectric Performance of $(Bi,Sb)_2Te_3$ Nanocomposites. *Nano Lett.* **2010**, *10*, 3283−3289.

(28) Muchler, L.; Casper, F.; Yan, B. H.; Chadov, S.; Felser, C. Topological Insulators and Thermoelectric Materials. *Phys. Status Solidi RRL* **2013**, *7*, 91−100.

(29) Shi, H. L.; Parker, D.; Du, M. H.; Singh, D. J. Connecting Thermoelectric Performance and Topological-Insulator Behavior: Bi_2Te_3 and Bi_2Te_2Se from First Principles. *Phys. Rev. Appl.* **2015**, *3*, 014004.

(30) Xu, Y.; Gan, Z. X.; Zhang, S. C. Enhanced Thermoelectric Performance and Anomalous Seebeck Effects in Topological Insulators. *Phys. Rev. Lett.* **2014**, *112*, 226801.

(31) Liang, J. H.; Cheng, L.; Zhang, J.; Liu, H. J.; Zhang, Z. Y. Maximizing the Thermoelectric Performance of Topological Insulator Bi_2Te_3 Films in the Few−Quintuple Layer Regime. *Nanoscale* **2016**, *8*, 8855−8862.

(32) Xia, Y.; Qian, D.; Hsieh, D.; Wray, L.; Pal, A.; Lin, H.; Bansil, A.; Grauer, D.; Hor, Y. S.; Cava, R. J.; Hasan, M. Z. Observation of a Large−Gap Topological−Insulator Class with a Single Dirac Cone on the Surface. *Nat. Phys.* **2009**, *5*, 398−402.

(33) Hsieh, D.; Xia, Y.; Qian, D.; Wray, L.; Dil, J. H.; Meier, F.; Osterwalder, J.; Patthey, L.; Checkelsky, J. G.; Ong, N. P.; Fedorov, A. V.; Lin, H.; Bansil, A.; Grauer, D.; Hor, Y. S.; Cava, R. J.; Hasan, M. Z. A Tunable Topological Insulator in the Spin Helical Dirac Transport Regime. *Nature* **2009**, *460*, 1101−1105.

(34) Sun, Y. F.; Cheng, H.; Gao, S.; Liu, Q. H.; Sun, Z. H.; Xiao, C.; Wu, C. Z.; Wei, S. P.; Xie, Y. Atomically Thick Bismuth Selenide Freestanding Single Layers Achieving Enhanced Thermoelectric Energy Harvesting. *J. Am. Chem. Soc.* **2012**, *134*, 20294−20297.

(35) Zhang, J. S.; Feng, X.; Xu, Y.; Guo, M. H.; Zhang, Z. C.; Ou, Y. B.; Feng, Y.; Li, K.; Zhang, H. J.; Wang, L. L.; Chen, X.; Gan, Z. X.; Zhang, S. C.; He, K.; Ma, X. C.; Xue, Q. K.; Wang, Y. Y. Disentangling the Magnetoelectric and Thermoelectric Transport in Topological Insulator Thin Films. *Phys. Rev. B: Condens. Matter Mater. Phys.* **2015**, *91*, 075431.

(36) Lee, S.; Hippalgaonkar, K.; Yang, F.; Hong, J.; Ko, C.; Suh, J.; Liu, K.; Wang, K.; Urban, J. J.; Zhang, X.; Dames, C.; Hartnoll, S. A.; Delaire, O.; Wu, J. Anomalously Low Electronic Thermal Conductivity in Metallic Vanadium Dioxide. *Science* **2017**, *355*, 371.

(37) Snyder, G. J.; Ursell, T. S. Thermoelectric Efficiency and Compatibility. *Phys. Rev. Lett.* **2003**, *91*, 148301.

(38) Taskin, A. A.; Sasaki, S.; Segawa, K.; Ando, Y. Manifestation of Topological Protection in Transport Properties of Epitaxial Bi_2Se_3 Thin Films. *Phys. Rev. Lett.* **2012**, *109*, 066803.

(39) Luo, X.; Sullivan, M. B.; Quek, S. Y. First−Principles Investigations of the Atomic, Electronic, and Thermoelectric Properties of Equilibrium and Strained Bi_2Se_3 and Bi_2Te_3 Including Van Der Waals Interactions. *Phys. Rev. B: Condens. Matter Mater. Phys.* **2012**, *86*, 184111.

(40) Goldsmid, H. J. *Introduction to Thermoelectricity*; Springer: New York, 2009.

(41) Aschcroft, N. W.; Mermin, N. D. *Solid State Physics*; Holt−Saunders: Philadelphia, 1976.

(42) Mahan, G. D.; Sofo, J. O. The Best Thermoelectric. *Proc. Natl. Acad. Sci. U. S. A.* **1996**, *93*, 7436−7439.

(43) Snyder, G. J.; Snyder, A. H. Figure of Merit ZT of a Thermoelectric Device Defined from Materials Properties. *Energy Environ. Sci.* **2017**, *10*, 2280−2283.

(44) Hsiung, T. C.; Mou, C. Y.; Lee, T. K.; Chen, Y. Y. Surface−Dominated Transport and Enhanced Thermoelectric Figure of Merit in Topological Insulator $Bi_{1.5}Sb_{0.5}Te_{1.7}Se_{1.3}$. *Nanoscale* **2015**, *7*, 518−523.

(45) Kresse, G.; Furthmuller, J. Efficiency of Ab−Initio Total Energy Calculations for Metals and Semiconductors Using a Plane−Wave Basis Set. *Comput. Mater. Sci.* **1996**, *6*, 15−50.

(46) Kresse, G. Ab Initio Molecular Dynamics for Liquid Metals. *J. Non-Cryst. Solids* **1995**, *192-193*, 222−229.

(47) Kresse, G.; Furthmuller, J. Efficient Iterative Schemes for *Ab Initio* Total−Energy Calculations Using a Plane−Wave Basis Set. *Phys. Rev. B: Condens. Matter Mater. Phys.* **1996**, *54*, 11169−11186.

(48) Perdew, J. P.; Chevary, J. A.; Vosko, S. H.; Jackson, K. A.; Pederson, M. R.; Singh, D. J.; Fiolhais, C. Atoms, Molecules, Solids, and Surfaces: Applications of the Generalized Gradient Approximation for Exchange and Correlation. *Phys. Rev. B: Condens. Matter Mater. Phys.* **1992**, *46*, 6671−6687.

(49) Perdew, J. P.; Wang, Y. Pair−Distribution Function and Its Coupling−Constant Average for the Spin−Polarized Electron−Gas. *Phys. Rev. B: Condens. Matter Mater. Phys.* **1992**, *46*, 12947−12954.

(50) Grimme, S.; Antony, J.; Ehrlich, S.; Krieg, H. A Consistent and Accurate *Ab Initio* Parametrization of Density Functional Dispersion Correction (DFT−D) for the 94 Elements H−Pu. *J. Chem. Phys.* **2010**, *132*, 154104.

(51) Grimme, S.; Ehrlich, S.; Goerigk, L. Effect of the Damping Function in Dispersion Corrected Density Functional Theory. *J. Comput. Chem.* **2011**, *32*, 1456−1465.

(52) Callaway, J. Model for Lattice Thermal Conductivity at Low Temperatures. *Phys. Rev.* **1959**, *113*, 1046−1051.

(53) Navratil, J.; Horak, J.; Plechacek, T.; Kamba, S.; Lost'ak, P.; Dyck, J. S.; Chen, W.; Uher, C. Conduction Band Splitting and Transport Properties of Bi_2Se_3. *J. Solid State Chem.* **2004**, *177*, 1704−1712.